Translational value of choroid plexus imaging for tracking neuroinflammation in mice and humans

Vinzenz Fleischer[a,1], Gabriel Gonzalez-Escamilla[a,1], Dumitru Ciolac[a], Philipp Albrecht[b], Patrick Küry[b], Joel Gruchot[b], Michael Dietrich[b], Christina Hecker[b], Thomas Müntefering[b], Stefanie Bock[c], Mohammadsaleh Oshaghi[a], Angela Radetz[a], Manuela Cerina[c], Julia Krämer[c], Lydia Wachsmuth[d], Cornelius Faber[d], Hans Lassmann[e], Tobias Ruck[b], Sven G. Meuth[b,c,2], Muthuraman Muthuraman[a,2], and Sergiu Groppa[a,2,3]

[a]Department of Neurology, Focus Program Translational Neuroscience, Rhine Main Neuroscience Network, University Medical Center of the Johannes Gutenberg University Mainz, 55131 Mainz, Germany; [b]Department of Neurology, Medical Faculty, Heinrich-Heine-University, 40225 Düsseldorf, Germany; [c]Department of Neurology, University Hospital Münster, Westfälische Wilhelms-University Münster, 48149 Münster Germany; [d]Clinic of Radiology, University Hospital Münster, 48149 Münster, Germany; and [e]Department of Neuroimmunology, Center for Brain Research, Medical University Vienna, A-1090 Vienna, Austria

Edited by Lawrence Steinman, Stanford University School of Medicine, Stanford, CA, and approved July 28, 2021 (received for review December 8, 2020)

Neuroinflammation is a pathophysiological hallmark of multiple sclerosis and has a close mechanistic link to neurodegeneration. Although this link is potentially targetable, robust translatable models to reliably quantify and track neuroinflammation in both mice and humans are lacking. The choroid plexus (ChP) plays a pivotal role in regulating the trafficking of immune cells from the brain parenchyma into the cerebrospinal fluid (CSF) and has recently attracted attention as a key structure in the initiation of inflammatory brain responses. In a translational framework, we here address the integrity and multidimensional characteristics of the ChP under inflammatory conditions and question whether ChP volumes could act as an interspecies marker of neuroinflammation that closely interrelates with functional impairment. Therefore, we explore ChP characteristics in neuroinflammation in patients with multiple sclerosis and in two experimental mouse models, cuprizone diet-related demyelination and experimental autoimmune encephalomyelitis. We demonstrate that ChP enlargement—reconstructed from MRI—is highly associated with acute disease activity, both in the studied mouse models and in humans. A close dependency of ChP integrity and molecular signatures of neuroinflammation is shown in the performed transcriptomic analyses. Moreover, pharmacological modulation of the blood–CSF barrier with natalizumab prevents an increase of the ChP volume. ChP enlargement is strongly linked to emerging functional impairment as depicted in the mouse models and in multiple sclerosis patients. Our findings identify ChP characteristics as robust and translatable hallmarks of acute and ongoing neuroinflammatory activity in mice and humans that could serve as a promising interspecies marker for translational and reverse-translational approaches.

multiple sclerosis | choroid plexus | neuroinflammation | disease activity

The choroid plexus (ChP), which extends along the floor of the lateral ventricles and the roof of the third and fourth ventricles (1), is a highly vascularized tissue that represents one key structure between the blood and the cerebrospinal fluid (CSF). The ChP plays an essential role in CSF production and brain waste clearance pathways, including the recently discovered glymphatic transport of CSF along the periarterial spaces (2–4). Additional functions of the ChP include maintenance of the neural parenchyma via secretion of neurotrophic factors and modulation of solute and immune cell trafficking across epithelial cells (5). Moreover, the ChP is involved in neuronal repair and restoration of function via gene expression and regulation of immune cell content (6–8).

Taken together, the blood–CSF barrier (BCSFB) in the ChP and the blood–brain barrier (BBB) regulate the entry of cells and solutes into the central nervous system (CNS). When these barriers and other regulatory mechanisms collapse, immune cells enter the CNS and may initiate neuroinflammatory diseases such as multiple sclerosis (MS), leading to demyelination and neuroaxonal degeneration. In line with this, inflammation and disruption of the ChP tissue architecture was detected in MS (9, 10). In postmortem studies, patients with MS showed an increased number of antigen-presenting cells in ChP stroma, as well as an infiltration of leukocytes from the periphery, a disruption of tight junctions in the ChP epithelium, and an endothelial overexpression of adhesion molecules involved in lymphocyte migration. Thus, the ChP can be considered one of the gateways for the migration of inflammatory cells into the brain, which indicates its structural importance in the pathogenesis of CNS diseases (11). These observations on a microscale potentially disrupt the morphology of the ChP also on a macroscale (12, 13). Despite the evidence available from neuropathological studies, we still lack an in vivo demonstration that the ChP is involved in the inflammatory process characterizing MS.

The cuprizone mouse model is a valuable tool to assess demyelination dynamics, since it induces early oligodendrocyte apoptosis, followed by astroglial and microglial activation and

Significance

Neuroinflammation is a hallmark of multiple sclerosis and is linked to neurodegeneration. This study provides pathophysiological insights into the cross-dependency between neuroinflammation and choroid plexus characteristics in both mice and humans. Our work relates an enlargement of choroid plexus volume to ongoing neuroinflammation and emerging clinical disability in two large cohorts of multiple sclerosis patients as well as in two mouse models, the cuprizone diet-related demyelination and the experimental autoimmune encephalomyelitis. Choroid plexus characterization as measured by high-resolution MRI thus represents a reliable and translatable interspecies marker for the quantification of neuroinflammation and disease trajectories that is strongly associated with functional outcomes.

Author contributions: G.G.-E., S.G.M., and S.G. designed research; V.F., G.G.-E., D.C., P.A., J.G., M.D., C.H., T.M., S.B., A.R., M.C., J.K., L.W., C.F., H.L., T.R., M.M., and S.G. performed research; V.F., G.G.-E., D.C., P.A., P.K., M.O., T.R., and M.M. analyzed data; and V.F. and G.G.-E. wrote the paper.

The authors declare no competing interest.

This article is a PNAS Direct Submission.

See online for related content such as Commentaries.

[1]V.F. and G.G.-E. contributed equally to this work.

[2]S.G.M., M.M., and S.G. contributed equally to this work.

[3]To whom correspondence may be addressed. Email: segroppa@uni-mainz.de.

This article contains supporting information online at https://www.pnas.org/lookup/suppl/doi:10.1073/pnas.2025000118/-/DCSupplemental.

Published September 3, 2021.

demyelination (14, 15). Although minor damage to the BBB has been described in this model (16), T and B cells are considered to play only a minor role during cuprizone-induced demyelination (17, 18). Moreover, immunohistochemistry has identified the presence of neuroinflammatory processes with anatomical affinity, particularly in the lining of the ChP (19). Thus, with the cuprizone model, two main aspects related to the MS pathology can be investigated: first, mechanisms underlying innate immune cell-driven myelin and axonal degeneration, and second, remyelination of the demyelinated axons (18).

On the other hand, experimental autoimmune encephalomyelitis (EAE)—the classic animal model of MS—is characterized by T cell and monocyte infiltration in the CNS associated with local inflammation and primary demyelination. In EAE, effector T cells enter the CSF from the leptomeninges or the ChP across activated vessels before spreading to the CNS tissues (20–23), suggesting that the ChP may be one of the initial sites of T cell entrance into the brain. In fact, it has been shown that the very late antigen-4 (VLA-4) and the melanoma cell adhesion molecule (MCAM) are important for transendothelial migration of T helper (Th)17 cells. VLA-4 plays a key role by mediating the initial rolling and adhesion steps of transmigration through interaction with its receptor, vascular cell adhesion molecule-1 (VCAM-1), expressed on endothelial cells upon inflammation (24). Targeting VLA-4 restricts most encephalitogenic T cells from migrating into the CNS (25), while blockade of MCAM more specifically inhibits Th17 cell migration into the CNS via the ChP endothelium (26).

Studies in mouse models mimicking aging in humans have provided further evidence that the ChP is involved in age-related immune cell recruitment, glial activation, and cognitive functioning (27, 28). These findings emphasize the impact of immune homeostasis within the ChP in shaping the brain's structural integrity and the clinical phenotype. However, while our understanding of the role of the ChP in brain homeostasis is growing, much less is known about its role in MS despite the intersection between ChP function and the neuroimmune axis. We hypothesized that inflammation through immune cell infiltration leads to an altered volume of the ChP and that MRI-derived ChP assessment provides a structural interspecies biomarker of inflammatory disease activity. Hence, this study aimed to investigate how ChP morphology is linked to disease activity in humans with MS and two experimental mouse models of CNS demyelination.

In this translational study, we identified an association between the ChP volumes as derived from high-field MRI, with clinical disability in a large cohort of MS patients over 3 y of annual follow-up. We validated our findings in a second cohort of treatment-naive MS patients at disease onset and after 4 y. Ultimately, we investigated the relationship between ChP volumes and CSF markers of BBB dysfunction and the effects of pharmacological inhibition of immune cell migration into the CNS on ChP volume changes. Moreover, we acquired MRI in the cuprizone-diet mouse model to determine whether ChP morphometry is related to demyelination and remyelination processes, depicting MS-like pathophysiology. Likewise, imaging in the EAE model served to evaluate the relationship of ChP morphology and functional impairment in mice. To evaluate the possible molecular mechanisms underlying ChP alterations, we further conducted immunohistochemistry and transcriptomic analyses from ChP tissue on both EAE and cuprizone models, which allow us to bridge the gap between ChP integrity and neuroinflammation.

Results

ChP Enlargement Is Associated with Disease Activity in MS. Bilateral ChP volumes were found to be enlarged in 330 MS patients when compared to healthy controls (HC) (Fig. 1*A* and *SI Appendix*, Figs. S1 and S2; n (HC) = 57; $t = 7$, $P < 0.001$). Larger ChP in MS patients were associated with the severity of clinical disability (assessed via Expanded Disability Status Scale [EDSS] scores] after adjusting for sex, age, disease duration, and intracranial volume (Fig. 2*A*) at baseline (standardized beta [β] = 0.170; $P = 0.004$) and after 4 y (β = 0.210; $P < 0.001$). These associations were also seen during the yearly follow-ups in between (*SI Appendix*, Fig. S3*A*). In addition, enlarged ChP volume was related with cortical thinning (Fig. 3*C*; $r = -0.328$, $P < 0.001$). Decreased cognitive performance measured with the Symbol Digit Modalities Test (SDMT), recognized as being particularly sensitive to the slowed processing of information that is commonly seen in MS, was also associated with ChP enlargement (Fig. 3*F*; $r = -0.375$; $P < 0.001$) after adjusting for sex, age, and intracranial volume.

Within the main MS cohort, a further comparison between patients with no evidence of disease activity (NEDA) and patients with disease activity (EDA) over a period of 2 y was conducted. Here, patients with EDA displayed larger ChP volumes at baseline compared to patients with NEDA (Mann–Whitney U test; $P < 0.001$). In comparison with healthy controls, both MS patients with NEDA and EDA showed significantly larger ChP volumes (Fig. 3*A*). Based on the hypothesis that ChP enlargement may mirror neuroinflammatory activity, we also assessed ChP morphometry with regard to demyelinating lesion load (high versus low T2-weighted hyperintense lesion volumes based on the median value). Our results demonstrated enlarged ChP volumes in patients with higher lesion load, while preserved ChP morphometry was observed in patients with a low degree of hyperintense lesions on T2-weighted images (Fig. 3*B*; Mann–Whitney U test; $P < 0.001$).

Finally, within the statistical framework, we applied structural equation modeling (SEM) to assess whether MRI-derived volumetric measurements of ChP represent a better biomarker related to EDSS scores in comparison to T1 contrast-enhancing lesions or new or enlarging T2 lesions. SEM identified the ChP volume as the strongest prognostic factor for EDSS scores (standardized coefficient [s] = 0.71, $P = 0.0005$). T1 contrast-enhancing lesions (s = 0.45, $P = 0.357$), as well as new or enlarging T2 lesions (s = 0.35, $P = 0.245$), did not reach significance in the designed predictive model.

ChP Enlargement in MS Is Confirmed in an Independent Validation Cohort. In the replication cohort of 235 treatment-naive MS patients at disease onset, enlarged ChP volume was concordantly associated with increased clinical disability after adjusting for sex, age, disease duration, and intracranial volume at baseline (β = 0.157; $P = 0.020$) and 4-y follow-up ($r = 0.289$, $P = 0.007$) (Fig. 2*B*). These positive associations were also seen after the 1- and 2-y follow-ups (*SI Appendix*, Fig. S3*B*). Consistently, as within the main cohort, in these patients, ChP enlargement was inversely associated with cortical thinning (Fig. 3*D*; $r = -0.277$, $P = 0.011$) after adjusting for sex, age, and intracranial volume.

ChP Enlargement Associates with Albumin in the CSF. Breakdown of the BBB is commonly seen in MS, yet it is not specific to the disease. Given the high concentration of albumin in plasma, it readily passes from the circulation into the CNS during BBB disruption and, thus, the albumin quotient (plasma to CSF) is used as an indicator of BBB dysfunction. Associations between enlarged ChP volumes were attested (*SI Appendix*, Table S3) with CSF albumin (Fig. 3*E*; $r = 0.281$, $P = 0.018$) and albumin quotient ($r = 0.292$, $P = 0.014$) but not for serum albumin ($r = 0.053$, $P = 0.662$). Notably, no associations between ChP volume and lymphocyte subsets (CD4+, CD8+, CD19+, and CD56+ cells) in the peripheral blood were found in patients (*SI Appendix*, Fig. S5 *A–D* and Table S4).

High-Efficacy Treatment Prevents ChP Enlargement. Untreated MS patients had larger ChP volumes at follow-up compared to baseline (*SI Appendix*, Fig. S4; $t = 0.011$, $P = 0.011$). MS patients under dimethyl fumarate (DMF) treatment had larger ChP volumes at follow-up compared to baseline (*SI Appendix*, Fig. S4; $t = 2.74$, $P = 0.0078$),

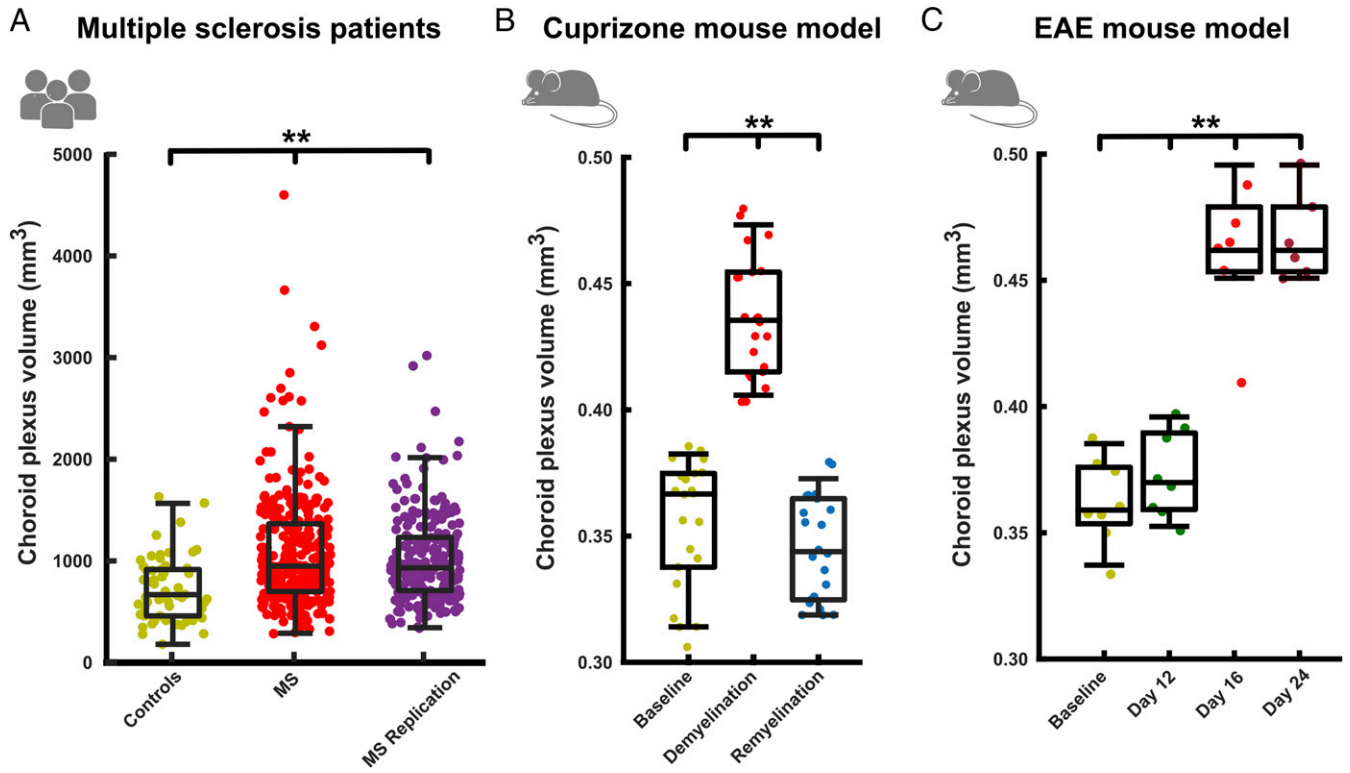

Fig. 1. Volumetric differences in the choroid plexus in human and mouse models. Box plots depicting choroid plexus volumes as derived from individual MRI. (*A*) In humans, enlarged volumes in MS patients with respect to HCs are evidenced. In mice, choroid plexus volumes showed a similar enlargement during the course of (*B*) the cuprizone-induced demyelination and (*C*) with increased disability during the course of the EAE mouse model. $^{**}P < 0.01$.

whereas patients under natalizumab (NAT) therapy showed stable ChP volumes at follow-up (*SI Appendix*, Fig. S4; $t = 1.26$, $P > 0.05$).

Cuprizone Mouse Model: ChP Volume Changes under De- and Remyelination. In our translational approach, we utilized a preclinical mouse model allowing the evaluation of demyelination and remyelination, which served to verify the volumetric changes of the ChP and its functional correlates (*SI Appendix*, Figs. S1 and S2). This animal model served to study consequences of myelin loss under transient pathological conditions. The comparison of the ChP volumes between untreated mice at baseline and after 2 wk of cuprizone diet depicted larger ChP volumes at the maximum of demyelination (Fig. 1*B*; $t = 4.578$, $P = 0.00023$). Subsequently, when myelin synthesis was reenabled by reintroduction of normal food after 6 wk, the mice presented significantly decreased ChP volume in comparison to the demyelination phase ($t = -3.567$, $P = 0.0048$). ChP morphology after remyelination induction was similar to that of the initially untreated period ($t = 1.897$, $P = 0.46$).

The open field (OF) test was applied in order to evaluate basal exploratory behavior via the distance traveled. Animals tested in the OF at baseline showed no significant correlation between the corresponding ChP volume and the distance traveled (*SI Appendix*, Fig. S6*A*; $r = 0.402$, $P = 0.063$). After 6 wk of cuprizone diet—at the peak of induced demyelination—the animals were measured again, and we observed a significant positive association between distance traveled and the ChP volume (*SI Appendix*, Fig. S6*B*; $r = 0.497$, $P = 0.018$). After diet withdrawal, the animals were again rescanned, and the traveled distance was measured. There was still a significant association between the anxiety-like behavior and the plexus volume at this time point (*SI Appendix*, Fig. S6*C*; $r = 0.652$, $P < 0.001$).

EAE Mouse Model: ChP Volume Changes under Autoimmune Inflammation. In addition to the intoxication model with cuprizone-induced demyelination, we employed the classic inflammatory EAE model to confirm our findings from the MS patient cohort in a second mouse model (*SI Appendix*, Fig. S1). Here, the administration of myelin-derived peptides causes an immune reaction against specific antigenic myelin proteins. In the EAE model, the peak of demyelination was reached 10 to 15 d after injection and was primarily confined to the spinal cord, although a certain degree of demyelination was also detected in the optic nerve, cerebral cortex, and cerebellum. Mice were scanned at baseline, day 12, day 16, and day 24, and ChP volumes were determined (Fig. 1*C*). ChP volume was significantly larger at day 24 ($t = 5.9$; $P = 0.00078$), day 16 ($t = 6.8$; $P = 0.00045$), and day 12 ($t = 3.4$; $P = 0.038$) in comparison to baseline.

We linked the ChP volume with the functional impairment in mice measured with the EAE score, a measure of disease severity characterizing motor deficits. We found positive associations between ChP morphology and the EAE severity scores at day 12 (*SI Appendix*, Fig. S6*D*; $r = 0.682$, $P = 0.023$), day 16 (*SI Appendix*, Fig. S6*E*; $r = 0.591$, $P = 0.042$), and day 24 (*SI Appendix*, Fig. S6*F*; $r = 0.664$, $P = 0.031$).

Enhanced Microglia Activation in the ChP at the Peak of the Disease in Both Mouse Models. In the cuprizone-diet mice (Fig. 4 *A–D*), the immunohistochemistry on ChP sections showed a significantly higher number of Iba1+ and Clec7a+ cells, as markers of microglial infiltration and activation, at the peak of demyelination in comparison to untreated mice ($P < 0.001$). A total of 4 wk after cuprizone diet withdrawal, the number of Iba1+ cells was comparable to naïve levels. Similarly, the number of CD3+ cells was significantly higher at the peak of demyelination ($P < 0.01$) but comparable to naïve mice 4 wk after diet withdrawal.

In EAE mice (Fig. 4 *E–H*), we found that the number of ChP Iba1+ cells was significantly higher at the peak of disease at day 14

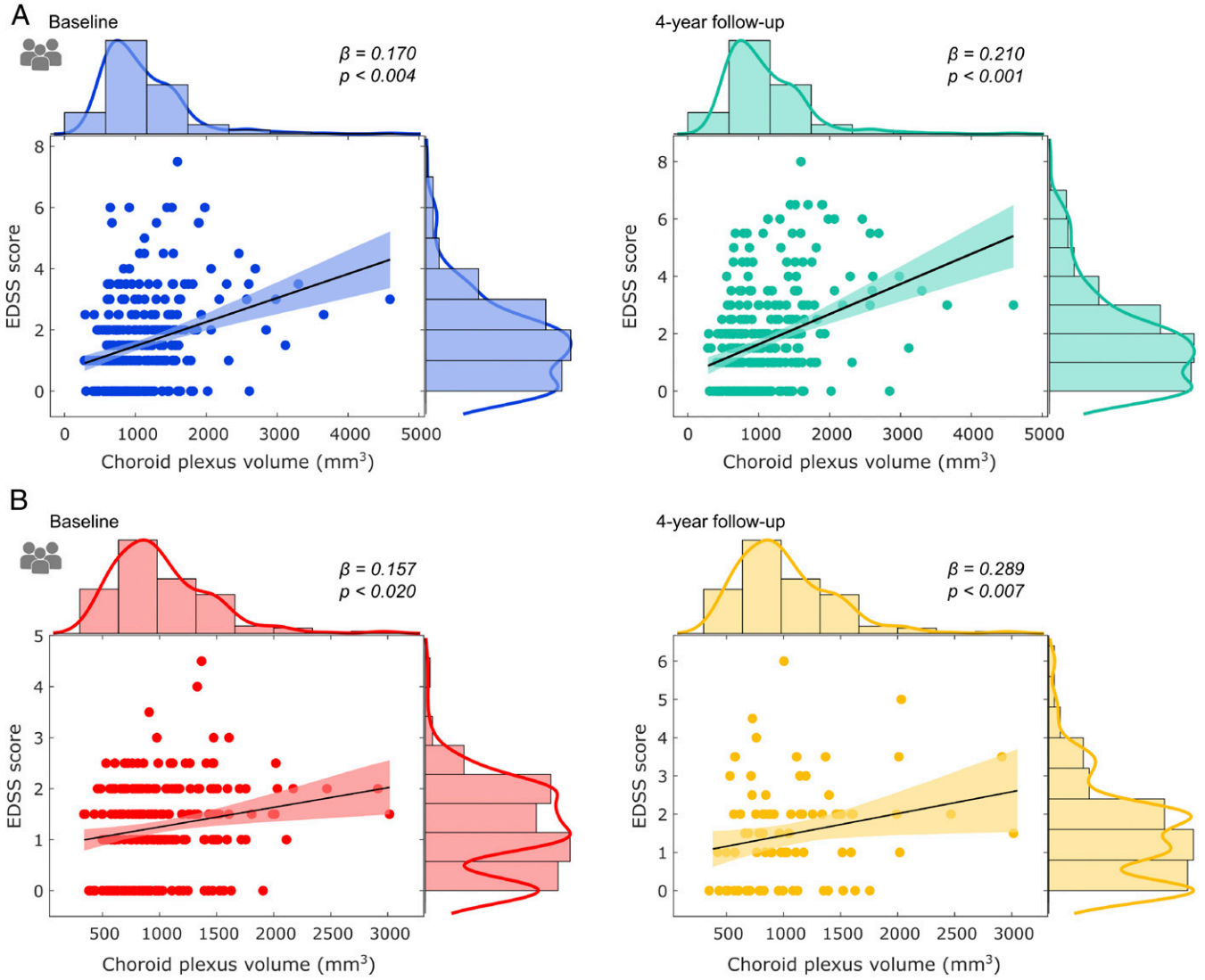

Fig. 2. Associations between clinical disability and choroid plexus enlargement in MS patients. Scatter plots depicting the association between choroid plexus volume and clinical disability, as measured with EDSS, in the study cohort (*A*), at baseline (blue) and at 4-y follow-up (green). In addition, the scatter plots derived from (*B*) the replication cohort are provided for baseline (red) and 4-y follow-up (yellow).

($P < 0.01$) and in the remission phase at day 21 ($P < 0.05$) after immunization in comparison to the naïve mice. In line with this, we observed a higher number of CD3+ cells in comparison to naïve mice 14 ($P < 0.01$) and 21 ($P < 0.05$) d after immunization.

ChP Volumes Relate to Glial Activity. Through immunohistochemistry, we observed positive associations between the number of cortical glial fibrillary acidic protein (GFAP+) positive cells, which is a specific marker for astrocyte content, and the ChP volume at baseline (Fig. 5*A*; $r = 0.560$, $P < 0.001$), full demyelination (Fig. 5*B*; $r = 0.630$, $P < 0.001$), and full remyelination (Fig. 5*C*; $r = 0.570$, $P < 0.001$). This observation supports the link between astrocyte activity and MRI-measured microstructural integrity in the gray matter regions. In addition, we were able to link the ChP volume to the ionized calcium-binding adapter molecule 1 (Iba1), a marker of microglia. At baseline, the association between ChP volume and Iba1 showed only a trend toward significance (Fig. 5*D*; $r = 0.380$, $P = 0.080$), whereas we found significant associations during full demyelination (Fig. 5*E*; $r = 0.600$, $P < 0.001$) and full remyelination (Fig. 5*F*; $r = 0.560$, $P < 0.001$).

ChP Transcriptomics Depict Neuroinflammation. The transcriptomic analyses from isolated ChP at peak of disease (cuprizone demyelination and EAE) showed that in comparison to baseline, gene expression in the ChP of both models revealed a shared signature of differentially up-regulated functional pathways primary related to neuroinflammation and cell-to-cell interactions, particularly a gene signature for genes associated with the regulation of leukocyte (T cell) adhesion, differentiation, and activation (Fig. 6).

Discussion

Over the last years, high-field structural MRI has become a powerful tool in deciphering and predicting specific brain pathology patterns (29, 30) and disease courses in inflammatory brain diseases such as MS (31). In particular, advances in brain imaging acquisition and postprocessing have improved the field and made tremendous contributions to our understanding of evolving neuroinflammation and neurodegeneration (32). The strength of MRI comes from its ability to provide quantifiable markers with high spatial accuracy that can trace disease trajectories both for research and clinical studies, focusing on both focal and widespread damage in the CNS (33).

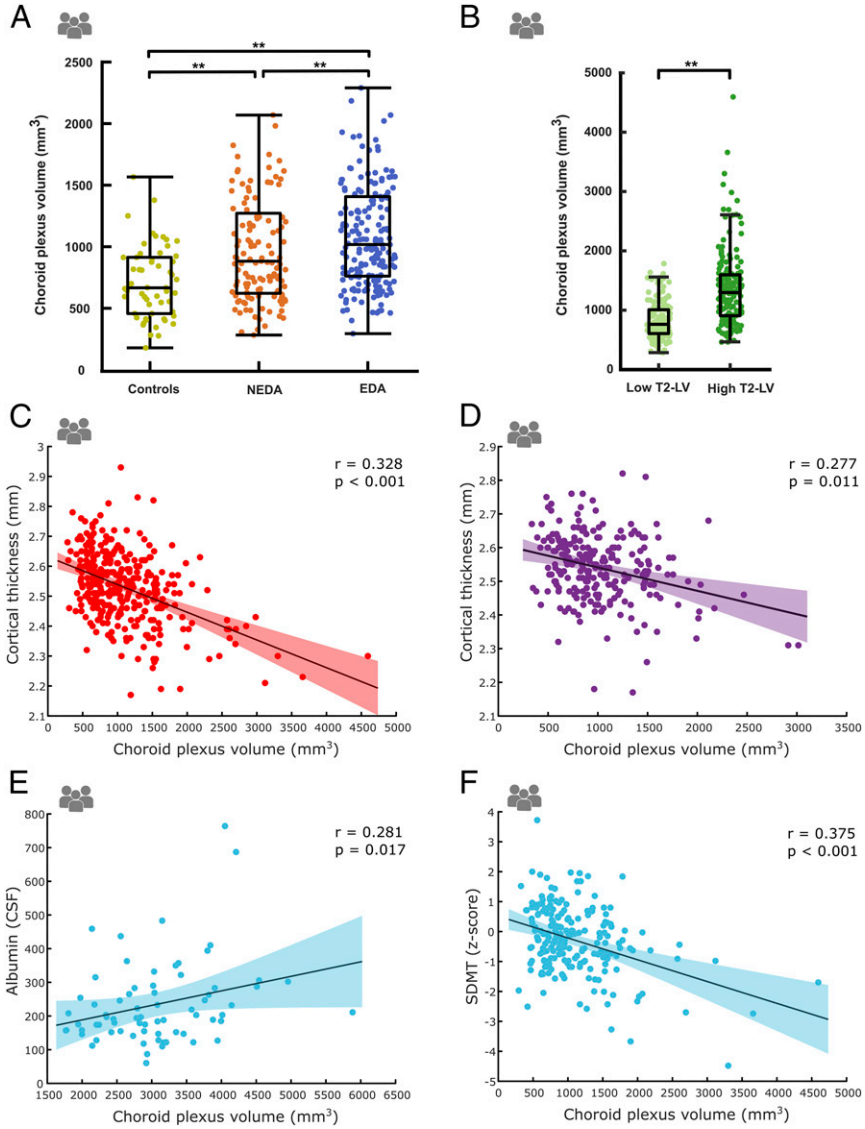

Fig. 3. Volumetric differences and associations of the choroid plexus with clinical, MRI, CSF, and cognitive measures. Choroid plexus volumes, derived from individual MRI in humans, depicting enlarged volumes in MS patients with EDA in comparison to MS patients with NEDA, each in comparison to healthy individuals' choroid plexus volume (*A*). Choroid plexus volumes depicting enlarged volumes in MS patients with high T2 lesion load in the MRI in comparison to patients with low T2 lesion load (*B*). Scatter plots depicting the association between choroid plexus volume and cortical thickness in the study cohort (*C*) and the replication cohort (*D*). Scatter plots depicting the association between choroid plexus volume and albumin in the CSF (*E*). Scatter plots depicting the association between choroid plexus volume and cognitive performance in the study cohort, as measured with the Symbol Digit Modalities Test (*F*). $^{**}P < 0.01$.

The current study identified an early association between enlargement of the ChP and disease severity in two large cohorts of MS patients, including both treatment-naïve patients and patients under immunomodulatory treatment. Predictive causal modeling through SEM confirmed that the ChP volumes were not only significant determinants that influence EDSS development in MS over time but also outperform conventional MRI biomarkers like T1 contrast-enhancing lesions and new T2 lesions. The translational analyses from two experimental in vivo animal models of acute neuroinflammation and de- and remyelination allow the establishment of volumetric ChP measurements as structural markers of neuroinflammation in mice. Thus, in both species, humans and mice, larger ChP volumes represent reproducible imaging surrogates of functional impairment, thus, suggesting that ChP can be used as a target in studies evaluating disease progression or therapy outcomes.

The underlying mechanisms leading to ChP enlargement with neuroinflammation appear to be complex and related to the interaction between the peripheral immune system and ChP stroma and epithelium cells. As shown in postmortem brain studies, the ChP of MS patients is characterized by a high proportion of MHC class II receptor T lymphocytes, which are indicative of active antigen presentation (10) by granulocyte and CD8+ T cell infiltration in the ChP stroma (34), and by overexpression of lymphocyte adhesion molecules by ChP endothelial cells (9). The presence of high levels of CD68+ activated macrophages in the ChP stroma and increased expression of VCAM-1 in the ChP vasculature (10) suggest an induction of endothelial immune proliferation and migration that might contribute to ChP enlargement. Accordingly, transcriptomic analyses on both EAE and cuprizone-diet models showed the involvement of up-regulated functional pathways involving T cell adhesion, differentiation, and activation as well as

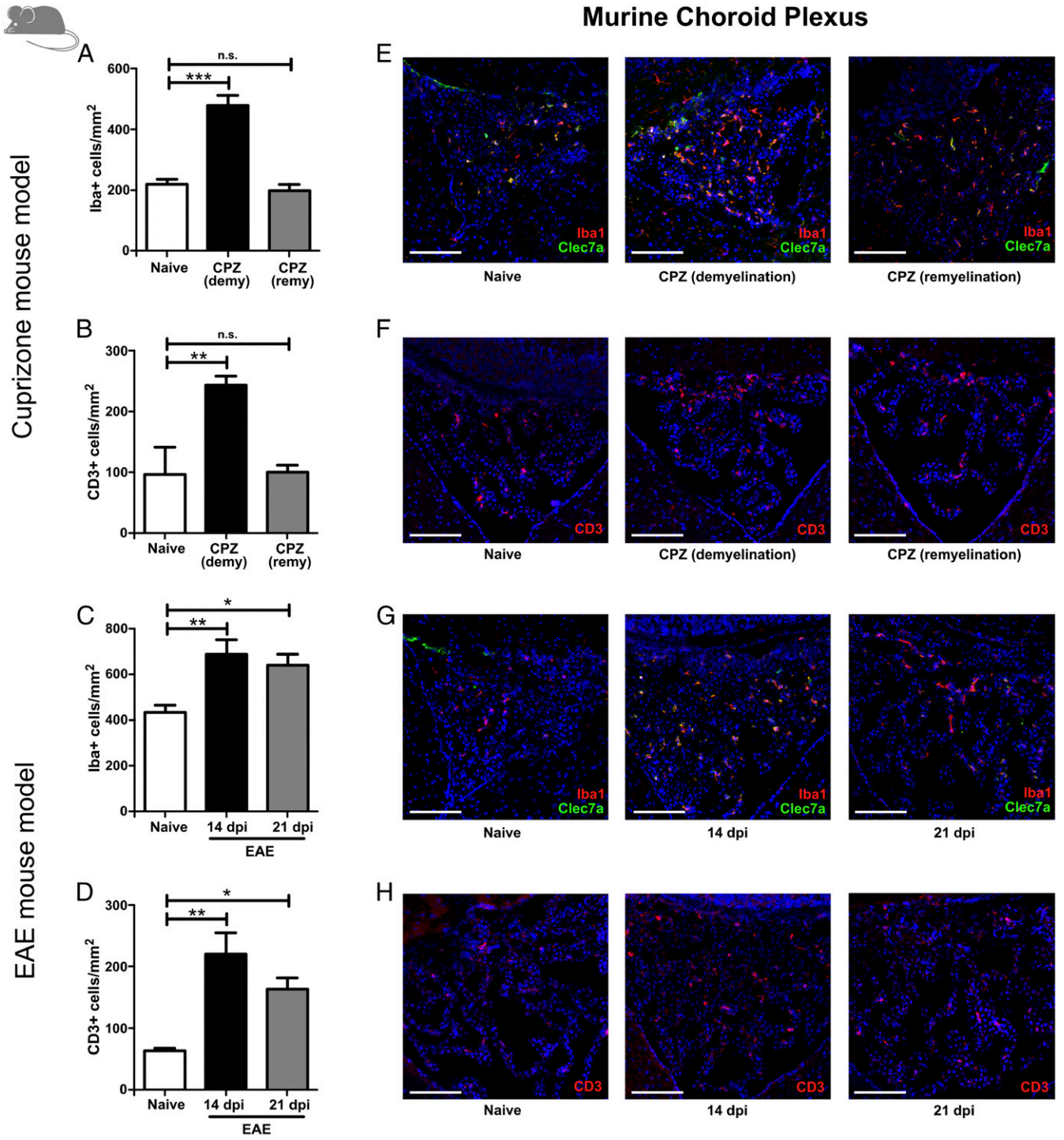

Fig. 4. Increased numbers of activated microglia and infiltrating T cells in the murine choroid plexus. Numbers of Iba1+ and CD3+ cells within the choroid plexus at different stages of the (*A* and *B*) cuprizone and (*C* and *D*) EAE mouse models were analyzed by immunohistochemistry. Representative images of the fluorescent stainings of the (*E* and *F*) cuprizone mice and (*G* and *H*) EAE mice depicting Iba1 (red)/Clec7a (green) positive activated microglia as well as CD3 (red) positive T cells. Nuclei were always counterstained with DAPI (blue). Statistical analysis was performed using ANOVA with Dunnett's post hoc test compared to naïve mice. $*P < 0.05$, $**P < 0.01$, $***P < 0.001$. (Scale bar: 100 μm.)

negative regulation of neuroimmune system during demyelination, in which VCAM-1 had a leading role, providing a direct link between enlarged ChP and neuroinflammation.

In the cuprizone model, ChP volume increase occurred during the demyelination phase as a transient enlargement; the ChP volume returned to baseline values after cuprizone diet withdrawal (remyelination). Although the cuprizone model does not require leukocyte migration into the CNS for the induction of demyelination (35, 36), the immune response to demyelination triggers the activation of CNS-resident cells (astrocytes and microglia) and the transmigration through the brain barriers (BBB and BCSFB) of peripheral immune cells (macrophages) into the areas of demyelination

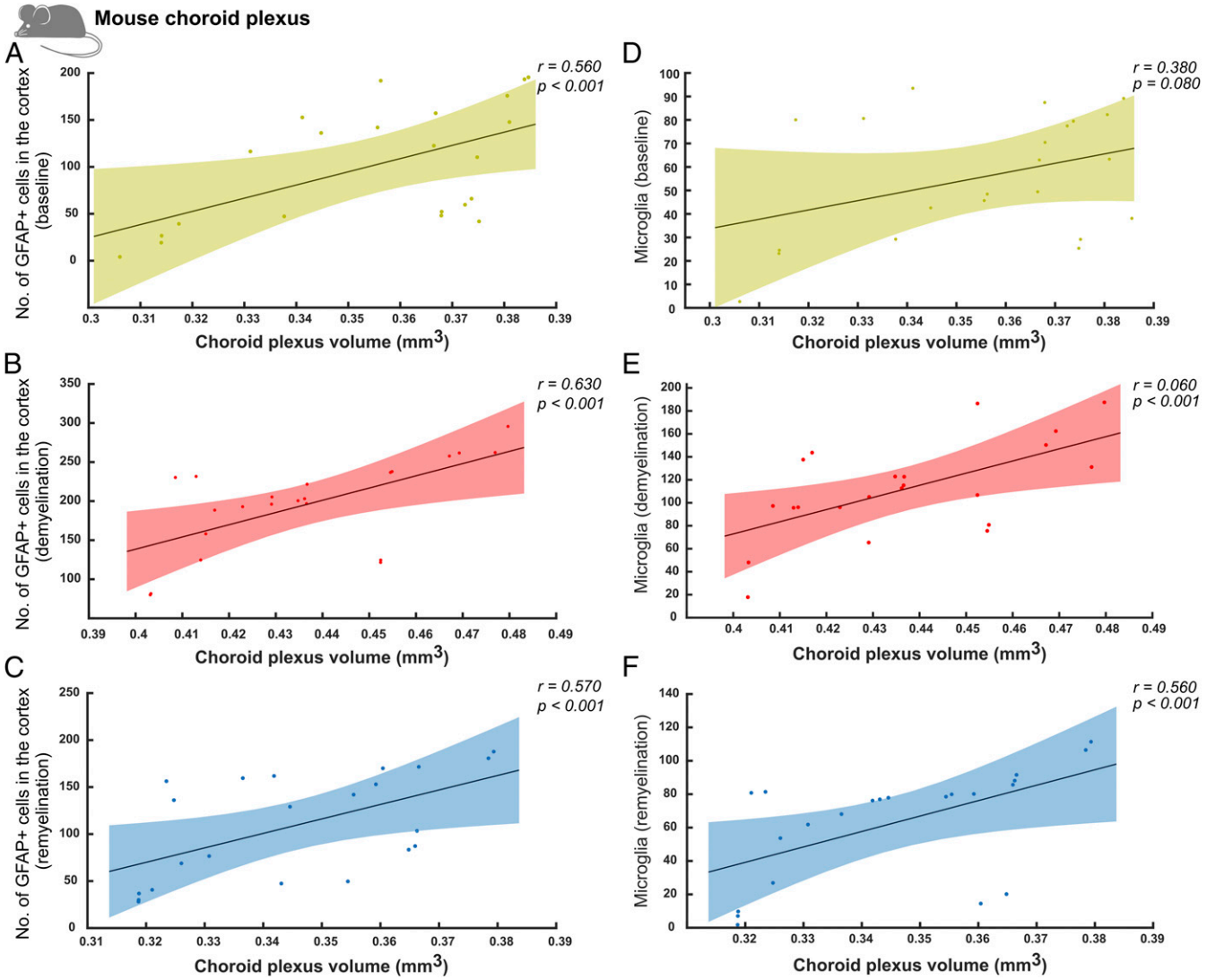

Fig. 5. Associations between choroid plexus volume and astrocyte and microglia counts in relation to the degree of myelination. Scatter plots in the left column illustrate the association between the number of GFAP+ cells in the cortex and the MRI-derived choroid plexus volume at baseline (*A*), demyelination (*B*), and remyelination (*C*) in the cuprizone mouse model. Right column scatter plots illustrate the association between the number of microglia cells in the cortex and the MRI-derived choroid plexus volume at baseline (*D*), demyelination (*E*), and remyelination (*F*) in the cuprizone mouse model.

(18, 37). In fact, the BBB permeability is increased at the peak of demyelination in the cuprizone model (16, 36). Astrocytes, which are involved in regulating endothelial function via their end feet (38), create a local inflammatory milieu that likely participates in destabilizing the BCSFB integrity mediated by down-regulation of tight junction proteins (16). Moreover, infiltrating cells from the periphery are not only detected in the cuprizone-induced lesions but also in regions distant from the areas of demyelination, including the ChP, leptomeninges, and perivascular regions (37, 39, 40). Thus, one explanation for ChP enlargement in the cuprizone model could be the secondary infiltration of immune cells from the periphery migrating through the ChP epithelium into the CNS in response to the stimuli derived from the cuprizone-damaged tissue. This hypothesis is in accordance with the up-regulation of genes in the ChP involved in cell adhesion and immune receptor activity in response to neuroinflammation in the cuprizone model.

Another mechanistic view of the depicted transcriptomic results could relate ChP enlargement to microglia activation, oxidative damage, and mitochondrial injury leading to hypoxia as a part of the cascade of events that lead to tissue injury (41, 42). Accordingly, in the cuprizone model, demyelination was evidenced to be accompanied by an overexpression of genes involved in oxidative and adenosine triphosphate (ATP)–dependent metabolic processes related to mitochondrial function. Thus, an overarching mechanism common to both EAE and cuprizone models could be related to mitochondrial energy failure within the ChP, most likely as a consequence of oxidative injury [possibly in the epithelial cells (41)] leading to a barrier dysfunction and ChP enlargement. A coexistence of those mechanisms with an immune response coinitiation, with ChP endothelium recruitment of T lymphocytes (which are normally confined to the CSF) causing an initial wave of Th17 cells (T cells mediating autoimmune demyelination) that enter the ChP stroma, is likely (21).

Furthermore, our results show an association between ChP enlargement and elevated CSF albumin and albumin quotient. ChP epithelial cells have a high cellular specificity for albumin transfer from the blood into the ventricular CSF (43). However, CSF albumin levels are dependent on the rate of albumin influx from distinct sources (e.g., transport from blood to CSF in the ChP, BBB leakage, and potential synthesis within the CNS) (44–46) as well as

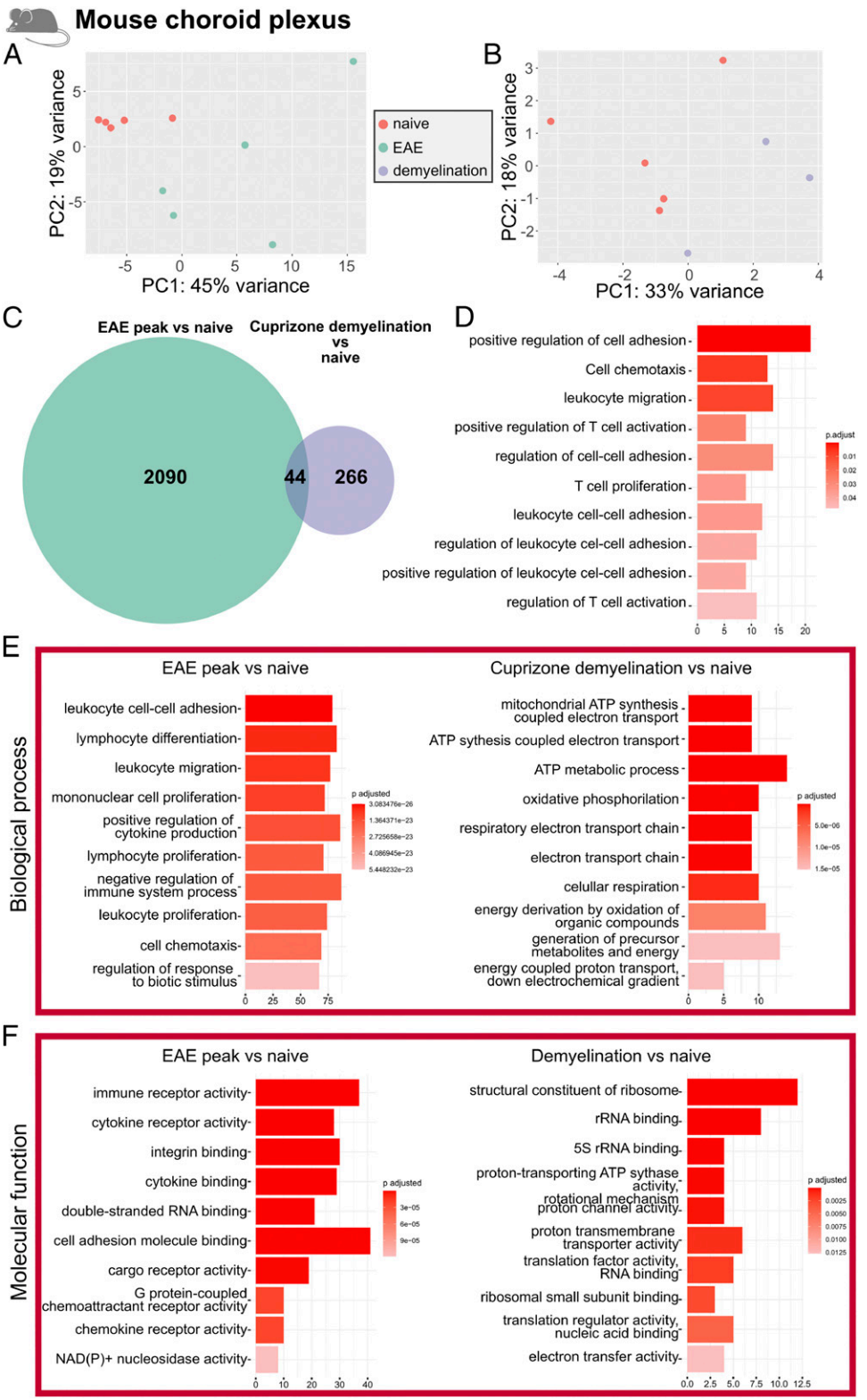

Fig. 6. Choroid plexus transcriptomics from the RNA sequencing. In *A*, the principal component analyses (PCA) show a good separation between the EAE peak ($n = 5$) and the naive EAE group ($n = 5$). The PCA analyses in the cuprizone model (*B*) show a very good cluster separation between the demyelination group ($n = 3$) and the naive group ($n = 5$). In *C*, the Venn diagram shows the differential expressed genes for the comparison between the EAE peak versus naive ($n = 2,090$) and cuprizone-diet induced demyelination versus naive ($n = 266$), and their shared gene expression ($n = 44$). In *D*, the common top 10 up-regulated biological processes pathways both in the EAE peak and the cuprizone demyelination groups are shown. In *E*, the up-regulated biological processes pathways for the two group comparisons, namely peak EAE versus naive and the cuprizone demyelination versus naive are shown, followed by the molecular function pathways in *F*, respectively. The up-regulated functional pathways shown here are all *P* adjusted < 0.05.

the rate of efflux (e.g., turnover of CSF) (47). During neuroinflammation, cellular alterations within the ChP (10) and reduced expression of tight junctions between the epithelial cells (48, 49) increase the permeability of the BCSFB for plasma constituents, including albumin. This influx might enlarge the volume of the cellular components of the ChP due to the interaction of colloid osmotic pressure and hydrostatic pressure on transmembrane water transport. However, changes in albumin transfer through the ChP, BBB leakage, and potentially increased CNS synthesis of albumin by microglia could all affect the CSF albumin concentration, suggesting that different pathways contribute to the observed association of albumin levels with ChP volume.

A recent study using brain tissue samples from patients with progressive MS proposed an important role of the ChP in immune homeostasis and indicated the occurrence of mild inflammatory processes within the ChP (34). The authors suggested that the ChP is only marginally involved in immune cell migration into the CNS in the neurodegeneration-dominated phase of the disease (34). However, we suggest that the early immune permeability of homeostasis response led to CNS tissue injury. In line with our observed relationship between enlarged ChP volumes and disability, previous studies suggested that in the EAE mouse model, inflammation in the ChP and CSF precedes the formation of brain and spinal cord inflammatory infiltrates as well as the development of demyelinating white matter lesions (50, 51). Moreover, the phenomenon that parenchymal CSF circulation is altered in EAE has received increasing attention in light of the recognition of the glymphatic system within the brain (4). The CSF flows from the ChP through the ventricles, enters the brain parenchyma via the perivascular spaces along arteries, and exits along the perivenous spaces to the cervical lymphatics, the arachnoid granulations, and the meningeal lymphatics (2, 52). Recently, an enlargement of ventricle volumes was demonstrated in EAE, which resolved upon clinical remission (53). This study showed how inflammatory processes at the ChP result in expansion of the cerebral ventricles and thus has implications for our findings. The transient ventricle enlargement shown by Millward et al. might be the consequence of an impaired CSF elimination associated with meningeal inflammation. However, these inflammatory processes likely interfere with the normal function of the ChP leading to altered CSF composition or CSF overproduction, as recently demonstrated in inflammation (54) that might drive both ventricle and ChP enlargement. Hence, the increased volume of the ChP could result from the concurrent activation of increased proliferation of ChP cells due to CSF hypersecretion (55), invasion of the ChP by nonresident immune cells (21), and possibly also edema (56).

Whereas in untreated and DMF-treated MS patients the ChP enlarges over time, we did not observe a significant ChP enlargement in NAT-treated MS patients. This finding offers two explanations. First, NAT is highly effective in the suppression of neuroinflammation and revealed a significantly better efficacy in comparison to untreated MS patients (57) as well as to DMF-treated MS patients (58). As NAT reduces inflammation more effectively, ChP volume reaches a plateau and ceases to further increase. Second, and related, the mode of action itself may also be responsible for the observed ChP volume stability in NAT-treated MS patients. NAT blocks the α4-β1 integrin on mononuclear leukocytes and decreases the binding to VCAM-1 (59, 60); thereby, NAT impedes transendothelial migration and the infiltration of leukocytes into the CNS (61). Leukocytes, in turn, have been reported to accumulate in the ChP by passing through the intercellular spaces between the ChP epithelial cells by the paracellular route (62).

Whether the ChP is a more sensitive and earlier marker of MS disease severity than other imaging markers and whether ChP enlargement is a consequence or an immediate cause of MS pathophysiology remains to be clarified. In MS, focal inflammation is known to be associated with widespread white matter pathology and brain topological reorganization (63, 64) as well as gray matter pathology (46, 65). Here, we extend previous observations by focusing on one of the key barriers, the BCSFB, compared to established surrogate markers of neuroinflammation in MS.

This study is not without limitations. First, the delineation of the ChP may not entirely capture its intricate structure. While algorithms for better delineating the ChP based on in vivo MRI data are under development (66), these commonly require complex computations or specialized acquisitions that are not available in clinical settings (67). However, manual delineation is very time consuming, and given the large amount of data, it becomes error prone. For this reason, we decided to employ an accurate automatic ChP parcellation technique, which has been widely utilized (68, 69) and is reliable compared to manual delineation (70). A second limitation is that the neuroinflammatory correlates of ChP were measured from routine peripheral and CSF samples. Despite the high spatial resolution in MRI, other imaging modalities, such as positron emission tomography, can visualize molecular characteristics in real time, and physiological parameters can be quantified in active disease processes within the ChP (71, 72). To overcome this disadvantage of structural MRI, we used a translational approach, which included cellular and imaging characterization allowing a direct comparison and replication of the presented findings.

Overall, this study provides evidence that from the early disease stages, volumetric alterations in the ChP occur in response to neuroinflammatory processes. Furthermore, enlarged ChP volume in MS patients is related to disease severity. This supports its crucial role in the regulation of the neuroimmune axis, which is related to brain homeostasis and interaction with the peripheral immune and inflammatory systems. The identification of enlarged ChP is a promising marker for an improved understanding and monitoring of disease pathology in MS. Larger volumes of the ChP can assist to identify patients at high risk for increased disease activity, who may benefit from early treatment.

Methods and Materials

Participants. Patients included in the main analyses and HCs were recruited in the Department of Neurology at the University Medical Center of the Johannes Gutenberg University Mainz in Germany. Patients with an initial diagnosis of either clinically isolated syndrome (CIS) (73) or relapsing-remitting MS (RRMS, according to 2010 McDonald criteria) (74) were prospectively recruited. After satisfying the study's inclusion criteria (75), patients were comprehensively examined and observed on an annual basis (for a 4-y follow-up period) according to a standardized assessment plan outlined elsewhere (76). Baseline 3T MRI datasets and 4-y clinical follow-up data were available for 330 patients, which were finally included into the analysis.

From these 330 patients, we further evaluated data of 71 patients (mean age ± SD 31.2 ± 9.4 y, 25 males) for whom albumin content in CSF and serum was available, 42 patients on DMF treatment (34.5 ± 9.0 y; 14 males) for whom immune cell subsets (CD4+, CD8+, CD19+, and CD56+ cells) data were available, and 36 patients (30.6 ± 8.1 y; 14 males) on NAT treatment.

Patients in the replication cohort were diagnosed according to the revised McDonald criteria 2010 (74). The following exclusion criteria were applied for all patients: any preexisting medical condition known to be associated with brain pathology; pregnancy; previous or current addiction to substances; relapses or systemic therapy with steroids (intravenous, intrathecal, or oral) within the month before the MRI examination; or a history of additional neurological or psychiatric disorders. Baseline 3T MRI datasets and 4-y clinical follow-up data were available for all 235 patients, which were finally included into the analysis.

The control group of 57 healthy individuals was randomly selected from our database from subjects without a neurological or a systemic immunological disease, who underwent a 1-y MRI assessment. Subjects were 18 y of age or older, in good general health, and were cognitively intact (i.e., able to understand the procedures and requirements and give informed consent).

Clinical Assessment. Each patient was clinically assessed by an experienced neurologist, and the EDSS score was determined at disease onset (study entrance), annually for 2 y, and after 4 y. The SDMT, a paper and pencil task, was used to measure cognitive processing speed (77).

Clinical Characteristics of the Participants. At baseline, within the main cohort of 330 patients (*SI Appendix*, Table S1), 63 (19%) patients were diagnosed with CIS and 267 (81%) patients already had definite RRMS; 232 females (70%)/98 males (30%); mean age 36.1 ± 10.8 y; median EDSS 1.5 (0 to 7.5). The mean disease duration was 38.3 ± 52.6 mo. EDSS scores significantly changed over the 3 y of follow-up ($P < 0.001$; nonparametric Friedman test).

Within the replication cohort (*SI Appendix*, Table S2), which was a treatment-naïve cohort, out of 235 patients (175 females [74%]/60 males [26%]; mean age 33.4 ± 9.6 y; median EDSS 1.5 [0 to 4.5]), 87 (37%) were diagnosed with CIS and 148 (63%) with RRMS. The mean disease duration was 6.5 ± 48.1 mo. The replication cohort included a subgroup of 87 patients with a clinical follow-up of 4 y, in whom the EDSS scores did not significantly change over the 4 y of follow-up ($P = 0.312$; nonparametric Mann–Whitney *U* test).

MRI Preprocessing and Parcellation. Detailed acquisition parameters are found in *SI Appendix, Supplementary Materials and Methods*. For all participants, automated parcellation of ChP in the lateral ventricles was performed from T1-w images using FreeSurfer (version 6.0; https://surfer.nmr.mgh.harvard.edu/). Technical details of the volume-based subcortical parcellation pipeline in FreeSurfer have been described elsewhere (78, 79). Briefly, a probabilistic atlas, built by manual labeling on a training dataset normalized to the MNI305 space resulting in a point-to-point correspondence between all training subjects, is used as parcellation prior for all brain regions. This atlas provides the probability of each brain region to belong to a given voxel, the probability of each brain region given the classification of neighboring voxels (neighborhood function), and the probability distribution function of voxel intensities, modeled as a normal distribution, for each brain region at each voxel. Then, newly introduced images are parceled by normalizing the new image to the common space and incorporating the subject-specific voxel intensities to find the optimal parcellation that maximizes the probability of observing the input data.

To ensure that the results including ChP volumes are not driven by other confounding factors, we also extracted ventricular volume (by combining left and right lateral ventricles) as well as total intracranial volume. The ventricular volume was further used as independent variable in other analyses.

Following brain ChP and ventricle parcellation by tiling the boundary of white matter mass, an initial white surface is created for each cerebral hemisphere, which is further refined following intensity gradients of the white matter and gray matter to generate the final gray–white surface. This surface is then extended to follow the intensity gradient of gray matter and CSF, leading to the creation of the pial surface. Finally, cortical thickness at each surface vertex is computed as the average distance from each vertex in the gray–white surface to the corresponding point in the pial surface (78).

Flow Cytometry. In the DMF group, lymphocyte subset counts of CD4+, CD8+, CD19+, and CD56+ cells were quantified with flow cytometry. Blood samples were collected from each patient at baseline and after follow-up. Fresh blood samples initially drawn into the ethylenediamine tetraacetic acid–containing tubes were then transferred to 5-mL fluorescence-activated cell sorting tubes and washed twice before erythrocytes were lysed with lysing solution at room temperature (RT). The cells were exposed to corresponding fluorochrome-conjugated monoclonal antibodies against CD4, CD8, CD19, and CD56. The absolute values of lymphocyte subsets were determined with TruCount beads (BD Biosciences).

Animal Models. For the model on demyelination and remyelination, experiments were performed on C57BL6J mice ($N = 10$; females, 9 wk old at the beginning of treatment, Envigo). All efforts were made to minimize stress for the animals in accordance with the Animal Research: Reporting of In Vivo Experiments guidelines (80). Food and water were available ad libitum. Cuprizone [bis(cyclohexylidenehydrazide)] was mixed with rodent pellet chow (0.2%). This compound is toxic for mature oligodendrocytes because it interferes with their internal mitochondrial metabolism and induces full demyelination after 6 wk of diet. Mice were measured at three time points: 1) baseline (before cuprizone diet), 2) after 6 wk of cuprizone diet (model of demyelination), and 3) after 6 wk of normal food reintroduction (model of remyelination). MRI was acquired at the three time points using a 9.4-Tesla small animal scanner with a mouse brain surface coil (Bio-Spec 94/20; Bruker BioSpin MRI GmbH). Mice were first anesthetized in a warmed Plexiglas box with 5% isoflurane (Baxter) in 1 L/min O_2. Isoflurane dosage was reduced to 1 to 1.5% in 1 L/min O_2/compressed air 30/70 vol% for positioning in the animal cradle and subsequent scanning. Stable physiology was controlled by continuous monitoring of body temperature via a rectal temperature probe (36.5 ± 0.5 °C) and by respiration rate (80 to 100 breaths/minute).

For the second animal model, EAE was induced by subcutaneous injection of 200 mg MOG peptide (Myelin Oligodendrocyte Glycoprotein Peptide Fragment 35 to 55; Charité) emulsified in complete Freund's adjuvant (Sigma-Aldrich) containing 200 mg *Mycobacterium tuberculosis* H37RA (Difco). Pertussis toxin (400 ng; Enzo Life Sciences) in 200 mL phosphate-buffered saline (PBS) was injected intraperitoneally at the day of immunization and 2 d later. Disease severity was scored daily in an anonymized fashion by two independent investigators using a scale from 0 to 5 (EAE score) as described elsewhere (81). In the EAE model, the peak of demyelination is reached after 10 to 15 d from the injection, primarily confined to the spinal cord, although a certain degree of demyelination is also detected in the optic nerve, cerebral cortex, and cerebellum. Mice were scanned at baseline, day 12, day 16, and day 24, and ChP volumes were determined with the aid of the Brain Extraction Toolkit.

Tissue Processing and Immunohistochemistry. EAE- and cuprizone-treated animals were deeply anesthetized with isoflurane and transcardially perfused with 20 mL cold PBS followed by 20 mL 4% paraformaldehyde. Brains were then removed and postfixed in the same fixative for 1 d at 4 °C, followed by 24 to 48 h cryoprotective dehydration in 30% sucrose at 4 °C. Afterward, brains were embedded in Tissue-Tek (Sakura Finetek Europe), frozen, and stored at −30 °C until preparation of 12-μm sections using a cryostat (Leica CM30510S). Sections were also stored at −30 °C.

For immunohistochemistry, sections of the ChP were thawed and left to dry for at least 15 min at RT. Before blocking, sections were rehydrated for 5 min in distilled water, transferred to −20 °C acetone (5 min), and washed in 1× Tris-buffered saline (TBS) (pH 7.6) and 1× TBS-T (TBS containing 0.02% Triton) for 5 min each. Blocking was performed with 3% normal goat serum (NGS) and 10% biotin-free bovine serum albumin (BSA; in TBS-T) for 30 min at RT, followed by application of the following antibodies (in 3% NGS and 10% BSA in TBS) and incubation overnight: rabbit anti-Iba1 (Wako Chemicals), rat anti-Clec7a (Dectin1; In Vivogen), and rabbit anti-CD3 (DAKO). Sections were washed two times for 5 min in TBS and incubated with DAPI and the species-appropriate fluorochrome-conjugated secondary antibody (1:500 in PBS) for 30 min at RT: goat anti-rabbit Alexa 594 (Thermo Fisher) and goat anti-rat Alexa 488 (Thermo Fisher). Images were taken using a Zeiss CLSM microscope 510 (CLSM 510, Zeiss); microglial infiltration and activation as well as T cell infiltration was quantified using the ImageJ BioVoxxel software (82) by an investigator anonymized to the experimental groups.

Images of slices containing the neocortex were collected from both hemispheres. A maximum of 11 slices per mouse were analyzed and considered as technical replicates for analysis of the cortex. For GFAP staining, images were acquired using 20- and 40-fold objectives and analyzed by counting the number of diaminobenzidine-positive cells per square millimeter.

Functional Testing in the Cuprizone Mouse Model. Behavioral responses to a novel environment were measured in an OF apparatus at baseline, demyelination, and remyelination. Animals were tested in the OF arena (35 × 40 × 40 cm), where, during the test, the mice were allowed to move freely around and explore the environment. In this study, the distance traveled was taken as a read-out of behavioral abnormalities (83) and expressed as a metric measurement (in centimeters), with longer distances indicating cognitive interference or anxiety-like behavior in the cuprizone diet.

RNA Sequencing and Analysis. Brains from naïve (baseline) as well as from EAE (days 14 and 21) and cuprizone-treated C57/Bl6 mice (peak demyelination and peak remyelination) were used to isolate ChP tissue. ChP tissue was manually dissected from the lateral, third, and fourth ventricles using an illuminated stereo microscope, as described elsewhere (84). Tissue from single mice was then immediately enzymatically digested in 300 μL Hank's balanced salt solution (HBSS) (Gibco; Catalog No. 14025-092) containing collagenase and dispase (Merck; Catalog No. 11097113001; concentration: 0.1 mg/mL) for 30 min at 37 °C on an orbital shaker. Subsequently, tissue was homogenized through a cell strainer (70-μm pore size) by an insulin syringe and washed with 600 μL HBSS solution. The sample was centrifuged at RT at 500 × *g* for 5 min. Supernatant was discarded, and the cell pellet was resuspended in 350 μL RLT buffer. For RNA isolation, Quiagen RNeasy Micro Kit (Catalog No. 74004) was used according to the manufacturer's instructions. Quality and amount of RNA were verified by NanoDrop and Bioanalyzer RNA 6,000 nano Kit (Agilent). Samples with RNA integrity number values >6.5 were used for RNA sequencing. NEBNext ribosomal RNA depletion was performed followed by NEBNext directional Ultra RNA II Library preparation and sequencing on NextSeq500 (Illumina) platform (75 cycles, high output version 2 kit). Raw sequencing data were filtered with the fastp program (85) to eliminate low-quality reads. Additionally, the parameters -g -x -p have been set for polyG

tail trimming, polyX tail trimming, and overrepresented sequence analysis. The quality of the trimmed data has been assured with fastqc. Afterward, the data were aligned to the latest reference genome (GRCm39 for mouse) using the long-read Spliced Transcript Alignment to a Reference aligner. Low-quality alignments have been filtered out using samtools, and the remaining high-quality alignments have been quantified using StringTie. The statistical analysis of the gene counts and principal component analyses were carried out with DESeq2 in R. The gene ontology analysis has been performed with clusterProfiler. The Venn diagram has been created with VennDiagram. The databases org.Hs.eg.db and org.Mm.eg.db have been used in R for annotating purposes.

Statistics. Statistical analyses were conducted in SPSS (version 23: IBM Corporation). First, the Shapiro–Wilk test was performed for the demographic and clinical variables to assess the distribution normality. Continuous and ordinal variables were compared using Student's *t* test and Mann–Whitney *U* test, respectively. Categorical variables were compared using a Pearson's χ^2 test.

The nonparametric Friedman test was used to explore longitudinal differences between the EDSS at the four time points in the study cohort. The Wilcoxon signed-rank test was used to test for differences between the EDSS at two time points in the replication cohort. Unless otherwise indicated, values are expressed as mean ± SD. ChP volumes were compared with the EDSS scores by multiple linear regression adjusting for age, sex, disease duration, and intracranial volume. Results from the regression model are given with standardized beta coefficients (β) and the corresponding *P* value; *P* values <0.05 were considered statistically significant. Lastly, an SEM was applied on MRI-derived markers (T1 contrast-enhancing lesions and new and/or enlarging T2 lesions) and the ChP volume to determine the marker that best predicted EDSS in our MS cohort (*SI Appendix, Supplementary Materials and Methods*). SEM was adjusted for sample size using the Root Mean Square Error of Approximation index, which improves precision without increasing bias (86).

Study Approval. For human participants, the study was approved by the local medical ethics committee of the State Medical Association (approval number 837.543.11 [8085]). Written informed consent in accordance with the Declaration of Helsinki was obtained from all subjects before participation. For animal experiments, the study was conducted in accordance with guidelines of local German authorities (Landesamt für Natur, Umwelt und Verbraucherschutz identification number: 84-02.04.2015.A585).

Data Availability. The data that support the findings of this study are included in this published article (and its *SI Appendix*), but restrictions apply to the availability of these data, which were used under license for the current study and so are not publicly available. Data are, however, available from the authors upon reasonable request.

ACKNOWLEDGMENTS. Parts of this research were conducted using the supercomputer Mogon and/or advisory services offered by Johannes Gutenberg University Mainz (http://hpc.uni-mainz.de/), which is a member of the Alliance for High Performance Computing in Rhineland Palatinate (http://www.ahrp.info/) and the Gauss Alliance e.V. Part of this research was supported by the core unit Preclinical Imaging eXperts, Interdisziplinäres Zentrum für Klinische Forschung Münster. We thank Dr. Cheryl Ernest and Christina Ruzene for proofreading and editing the manuscript. This study was supported by a grant from German Research Council (Grant CRC-TR-128).

1. D. Talhada *et al.*, The choroid plexus: Simple structure, complex functions. *J. Neurosci. Res.* **98**, 751–753 (2020).
2. A. Louveau *et al.*, Structural and functional features of central nervous system lymphatic vessels. *Nature* **523**, 337–341 (2015).
3. J. Kipnis, Multifaceted interactions between adaptive immunity and the central nervous system. *Science* **353**, 766–771 (2016).
4. J. J. Iliff *et al.*, A paravascular pathway facilitates CSF flow through the brain parenchyma and the clearance of interstitial solutes, including amyloid β. *Sci. Transl. Med.* **4**, 147ra111 (2012).
5. E. E. Benarroch, Choroid plexus–CSF system: Recent developments and clinical correlations. *Neurology* **86**, 286–296 (2016).
6. K. Baruch, M. Schwartz, CNS-specific T cells shape brain function via the choroid plexus. *Brain Behav. Immun.* **34**, 11–16 (2013).
7. F. Marques *et al.*, The choroid plexus in health and in disease: Dialogues into and out of the brain. *Neurobiol. Dis.* **107**, 32–40 (2017).
8. R. Spector, S. Robert Snodgrass, C. E. Johanson, A balanced view of the cerebrospinal fluid composition and functions: Focus on adult humans. *Exp. Neurol.* **273**, 57–68 (2015).
9. B. Engelhardt, K. Wolburg-Buchholz, H. Wolburg, Involvement of the choroid plexus in central nervous system inflammation. *Microsc. Res. Tech.* **52**, 112–129 (2001).
10. M. Vercellino *et al.*, Involvement of the choroid plexus in multiple sclerosis autoimmune inflammation: A neuropathological study. *J. Neuroimmunol.* **199**, 133–141 (2008).
11. E. H. Wilson, W. Weninger, C. A. Hunter, Trafficking of immune cells in the central nervous system. *J. Clin. Invest.* **120**, 1368–1379 (2010).
12. S. Kant, E. G. Stopa, C. E. Johanson, A. Baird, G. D. Silverberg, Choroid plexus genes for CSF production and brain homeostasis are altered in Alzheimer's disease. *Fluids Barriers CNS* **15**, 34 (2018).
13. E. Perez-Gracia, R. Blanco, M. Carmona, E. Carro, I. Ferrer, Oxidative stress damage and oxidative stress responses in the choroid plexus in Alzheimer's disease. *Acta Neuropathol.* **118**, 497–504 (2009).
14. D. Ciolac, S. A. Groppa, G. Gonzalez-Escamilla, "Translational characterization of the glia role in multiple sclerosis" in *Translational Methods for Multiple Sclerosis Research*, S. G. Meuth, S. Groppa, Eds. (Springer, 2021), pp. 61–76.
15. F. M. Glaser, T. Ruck, "Translational animal models for MS and related neuroimmunological disorders" in *Translational Methods for Multiple Sclerosis Research*, S. G. Meuth, S. Groppa, Eds. (Springer, 2021), pp. 13–27.
16. S. A. Berghoff *et al.*, Blood-brain barrier hyperpermeability precedes demyelination in the cuprizone model. *Acta Neuropathol. Commun.* **5**, 94 (2017).
17. Y. Wolf *et al.*, Microglial MHC class II is dispensable for experimental autoimmune encephalomyelitis and cuprizone-induced demyelination. *Eur. J. Immunol.* **48**, 1308–1318 (2018).
18. J. Zhan *et al.*, The cuprizone model: Dos and do nots. *Cells* **9**, 843 (2020).
19. A. Nack *et al.*, Expression of translocator protein and [18F]-GE180 ligand uptake in multiple sclerosis animal models. *Cells* **8**, 94 (2019).
20. A. Reboldi *et al.*, C-C chemokine receptor 6-regulated entry of TH-17 cells into the CNS through the choroid plexus is required for the initiation of EAE. *Nat. Immunol.* **10**, 514–523 (2009).
21. P. Kivisäkk *et al.*, Human cerebrospinal fluid central memory CD4+ T cells: Evidence for trafficking through choroid plexus and meninges via P-selectin. *Proc. Natl. Acad. Sci. U.S.A.* **100**, 8389–8394 (2003).
22. B. Engelhardt, R. M. Ransohoff, The ins and outs of T-lymphocyte trafficking to the CNS: Anatomical sites and molecular mechanisms. *Trends Immunol.* **26**, 485–495 (2005).
23. I. Bartholomäus *et al.*, Effector T cell interactions with meningeal vascular structures in nascent autoimmune CNS lesions. *Nature* **462**, 94–98 (2009).
24. O. Steiner *et al.*, Differential roles for endothelial ICAM-1, ICAM-2, and VCAM-1 in shear-resistant T cell arrest, polarization, and directed crawling on blood-brain barrier endothelium. *J. Immunol.* **185**, 4846–4855 (2010).
25. T. A. Yednock *et al.*, Prevention of experimental autoimmune encephalomyelitis by antibodies against alpha 4 beta 1 integrin. *Nature* **356**, 63–66 (1992).
26. J. Breuer *et al.*, Blockade of MCAM/CD146 impedes CNS infiltration of T cells over the choroid plexus. *J. Neuroinflammation* **15**, 236 (2018).
27. K. Baruch *et al.*, Aging-induced type I interferon response at the choroid plexus negatively affects brain function. *Science* **346**, 89–93 (2014).
28. K. Baruch *et al.*, CNS-specific immunity at the choroid plexus shifts toward destructive Th2 inflammation in brain aging. *Proc. Natl. Acad. Sci. U.S.A.* **110**, 2264–2269 (2013).
29. M. Calabrese *et al.*, Regional distribution and evolution of gray matter damage in different populations of multiple sclerosis patients. *PLoS One* **10**, e0135428 (2015).
30. M. D. Steenwijk *et al.*, Cortical atrophy patterns in multiple sclerosis are non-random and clinically relevant. *Brain* **139**, 115–126 (2016).
31. J. Krämer *et al.*, Imaging in mice and men: Pathophysiological insights into multiple sclerosis from conventional and advanced MRI techniques. *Prog. Neurobiol.* **182**, 101663 (2019).
32. O. Ciccarelli *et al.*, Pathogenesis of multiple sclerosis: Insights from molecular and metabolic imaging. *Lancet Neurol.* **13**, 807–822 (2014).
33. R. Cortese, S. Collorone, O. Ciccarelli, A. T. Toosy, Advances in brain imaging in multiple sclerosis. *Ther. Adv. Neurol. Disord.* **12**, 1756286419859722 (2019).
34. S. Rodríguez-Lorenzo *et al.*, Inflammation of the choroid plexus in progressive multiple sclerosis: Accumulation of granulocytes and T cells. *Acta Neuropathol. Commun.* **8**, 9 (2020).
35. A. V. Caprariello *et al.*, Biochemically altered myelin triggers autoimmune demyelination. *Proc. Natl. Acad. Sci. U.S.A.* **115**, 5528–5533 (2018).
36. J. Praet, C. Guglielmetti, Z. Berneman, A. Van der Linden, P. Ponsaerts, Cellular and molecular neuropathology of the cuprizone mouse model: Clinical relevance for multiple sclerosis. *Neurosci. Biobehav. Rev.* **47**, 485–505 (2014).
37. V. Yakimov *et al.*, Continuous cuprizone intoxication allows active experimental autoimmune encephalomyelitis induction in C57BL/6 mice. *Histochem. Cell Biol.* **152**, 119–131 (2019).
38. Y. Guo *et al.*, Pathogenic implications of cerebrospinal fluid barrier pathology in neuromyelitis optica. *Acta Neuropathol.* **133**, 597–612 (2017).
39. E. J. McMahon, K. Suzuki, G. K. Matsushima, Peripheral macrophage recruitment in cuprizone-induced CNS demyelination despite an intact blood-brain barrier. *J. Neuroimmunol.* **130**, 32–45 (2002).
40. C. Reinbach *et al.*, CD44 expression in the cuprizone model. *Brain Res.* **1745**, 146950 (2020).
41. G. R. Campbell *et al.*, Clonally expanded mitochondrial DNA deletions within the choroid plexus in multiple sclerosis. *Acta Neuropathol.* **124**, 209–220 (2012).

42. D. H. Mahad, B. D. Trapp, H. Lassmann, Pathological mechanisms in progressive multiple sclerosis. *Lancet Neurol.* **14**, 183–193 (2015).
43. S. A. Liddelow *et al*., Cellular specificity of the blood-CSF barrier for albumin transfer across the choroid plexus epithelium. *PLoS One* **9**, e106592 (2014).
44. S.-M. Ahn *et al*., Human microglial cells synthesize albumin in brain. *PLoS One* **3**, e2829 (2008).
45. T. Uher *et al*., Increased albumin quotient (QAlb) in patients after first clinical event suggestive of multiple sclerosis is associated with development of brain atrophy and greater disability 48 months later. *Mult. Scler.* **22**, 770–781 (2016).
46. J. Kroth *et al*., Increased cerebrospinal fluid albumin and immunoglobulin A fractions forecast cortical atrophy and longitudinal functional deterioration in relapsing-remitting multiple sclerosis. *Mult. Scler.* **25**, 338–343 (2019).
47. S. M. LeVine, Albumin and multiple sclerosis. *BMC Neurol.* **16**, 47 (2016).
48. H. Wolburg, K. Wolburg-Buchholz, B. Engelhardt, "Involvement of tight junctions during transendothelial migration of mononuclear cells in experimental autoimmune encephalomyelitis" in *Neuroinflammation in Stroke*, U. Dirnagl, B. Elger, Eds. (Ernst Schering Research Foundation Workshop, Springer, 2004), vol. 47, pp. 17–38.
49. G. L. Suidan, J. R. Mcdole, Y. Chen, I. Pirko, A. J. Johnson, Induction of blood brain barrier tight junction protein alterations by CD8 T cells. *PLoS One* **3**, e3037 (2008).
50. D. A. Brown, P. E. Sawchenko, Time course and distribution of inflammatory and neurodegenerative events suggest structural bases for the pathogenesis of experimental autoimmune encephalomyelitis. *J. Comp. Neurol.* **502**, 236–260 (2007).
51. C. Schmitt, N. Strazielle, J. F. Ghersi-Egea, Brain leukocyte infiltration initiated by peripheral inflammation or experimental autoimmune encephalomyelitis occurs through pathways connected to the CSF-filled compartments of the forebrain and midbrain. *J. Neuroinflammation* **9**, 187 (2012).
52. J. J. Iliff *et al*., Brain-wide pathway for waste clearance captured by contrast-enhanced MRI. *J. Clin. Invest.* **123**, 1299–1309 (2013).
53. J. M. Millward *et al*., Transient enlargement of brain ventricles during relapsing-remitting multiple sclerosis and experimental autoimmune encephalomyelitis. *JCI Insight* **5**, e140040 (2020).
54. J. K. Karimy *et al*., Inflammation-dependent cerebrospinal fluid hypersecretion by the choroid plexus epithelium in posthemorrhagic hydrocephalus. *Nat. Med.* **23**, 997–1003 (2017).
55. B. Z. Barkho, E. S. Monuki, Proliferation of cultured mouse choroid plexus epithelial cells. *PLoS One* **10**, e0121738 (2015).
56. E. Cardia *et al*., Morphological modifications of the choroid plexus in a rodent model of acute ventriculitis induced by gram-negative liquoral sepsis. Possible implications in the pathophysiology of hypersecretory hydrocephalus. *Childs Nerv. Syst.* **11**, 511–516 (1995).
57. C. H. Polman *et al*.; AFFIRM Investigators, A randomized, placebo-controlled trial of natalizumab for relapsing multiple sclerosis. *N. Engl. J. Med.* **354**, 899–910 (2006).
58. B. L. Vollmer *et al*., Natalizumab versus fingolimod and dimethyl fumarate in multiple sclerosis treatment. *Ann. Clin. Transl. Neurol.* **6**, 252–262 (2018).
59. A. Mathias *et al*., Impaired T-cell migration to the CNS under fingolimod and dimethyl fumarate. *Neurol. Neuroimmunol. Neuroinflamm.* **4**, e401 (2017).
60. M. Skarica, C. Eckstein, K. A. Whartenby, P. A. Calabresi, Novel mechanisms of immune modulation of natalizumab in multiple sclerosis patients. *J. Neuroimmunol.* **235**, 70–76 (2011).
61. R. R. Lobb, M. E. Hemler, The pathophysiologic role of alpha 4 integrins in vivo. *J. Clin. Invest.* **94**, 1722–1728 (1994).
62. C. Kaur, G. Rathnasamy, E. A. Ling, The choroid plexus in healthy and diseased brain. *J. Neuropathol. Exp. Neurol.* **75**, 198–213 (2016).
63. V. Fleischer *et al*., Graph theoretical framework of brain networks in multiple sclerosis: A review of concepts. *Neuroscience* **403**, 35–53 (2019).
64. M. Muthuraman *et al*., Covarying patterns of white matter lesions and cortical atrophy predict progression in early MS. *Neurol. Neuroimmunol. Neuroinflamm.* **7**, e681 (2020).
65. R. Magliozzi *et al*., The CSF profile linked to cortical damage predicts multiple sclerosis activity. *Ann. Neurol.* **88**, 562–573 (2020).
66. E. Tadayon *et al*.; Alzheimer's Disease Neuroimaging Initiative, Improving choroid plexus segmentation in the healthy and diseased brain: Relevance for Tau-PET imaging in dementia. *J. Alzheimers Dis.* **74**, 1057–1068 (2020).
67. B. Alicioglu, G. Yilmaz, O. Tosun, N. Bulakbasi, Diffusion-weighted magnetic resonance imaging in the assessment of choroid plexus aging. *Neuroradiol. J.* **30**, 490–495 (2017).
68. H. Murck *et al*., Ventricular volume, white matter alterations and outcome of major depression and their relationship to endocrine parameters – A pilot study. *World J. Biol. Psychiatry* **22**, 104–118 (2021).
69. G. Zhou, J. Hotta, M. K. Lehtinen, N. Forss, R. Hari, Enlargement of choroid plexus in complex regional pain syndrome. *Sci. Rep.* **5**, 14329 (2015).
70. P. Lizano *et al*., Association of choroid plexus enlargement with cognitive, inflammatory, and structural phenotypes across the psychosis spectrum. *Am. J. Psychiatry* **176**, 564–572 (2019).
71. C. M. Lee *et al*., 18F-flortaucipir binding in choroid plexus: Related to race and hippocampus signal. *J. Alzheimers Dis.* **62**, 1691–1702 (2018).
72. S.L. Baker, T.M. Harrison, A. Maass, R. La Joie, W.J. Jagust, Effect of off-target binding on (18)F-flortaucipir variability in healthy controls across the life span. *J. Nucl. Med.* **60**, 1444–1451 (2019).
73. F. Barkhof *et al*., Comparison of MRI criteria at first presentation to predict conversion to clinically definite multiple sclerosis. *Brain* **120**, 2059–2069 (1997).
74. C. H. Polman *et al*., Diagnostic criteria for multiple sclerosis: 2010 revisions to the McDonald criteria. *Ann. Neurol.* **69**, 292–302 (2011).
75. A. Johnen *et al*., Can we predict cognitive decline after initial diagnosis of multiple sclerosis? Results from the German National early MS cohort (KKNMS). *J. Neurol.* **266**, 386–397 (2019).
76. O. von Bismarck *et al*., Treatment choices and neuropsychological symptoms of a large cohort of early MS. *Neurol. Neuroimmunol. Neuroinflamm.* **5**, e446 (2018).
77. L. Strober *et al*.; Multiple Sclerosis Outcome Assessments Consortium (MSOAC), Symbol digit modalities test: A valid clinical trial endpoint for measuring cognition in multiple sclerosis. *Mult. Scler.* **25**, 1781–1790 (2019).
78. B. Fischl, FreeSurfer. *Neuroimage* **62**, 774–781 (2012).
79. R. S. Desikan *et al*., An automated labeling system for subdividing the human cerebral cortex on MRI scans into gyral based regions of interest. *Neuroimage* **31**, 968–980 (2006).
80. C. Kilkenny, W. Browne, I. C. Cuthill, M. Emerson, D. G. Altman; NC3Rs Reporting Guidelines Working Group, Animal research: Reporting in vivo experiments: The ARRIVE guidelines. *Br. J. Pharmacol.* **160**, 1577–1579 (2010).
81. S. Bittner *et al*., Endothelial TWIK-related potassium channel-1 (TREK1) regulates immune-cell trafficking into the CNS. *Nat. Med.* **19**, 1161–1165 (2013).
82. C. A. Schneider, W. S. Rasband, K. W. Eliceiri, NIH Image to ImageJ: 25 years of image analysis. *Nat. Methods* **9**, 671–675 (2012).
83. M. Cerina *et al*., Myelination- and immune-mediated MR-based brain network correlates. *J. Neuroinflammation* **17**, 1–16 (2020).
84. T. R. Menheniott, M. Charalambous, A. Ward, Derivation of primary choroid plexus epithelial cells from the mouse. *Methods Mol. Biol.* **633**, 207–220 (2010).
85. S. Chen, Y. Zhou, Y. Chen, J. Gu, fastp: An ultra-fast all-in-one FASTQ preprocessor. *Bioinformatics* **34**, i884–i890 (2018).
86. K. Kelley, K. Lai, Accuracy in parameter estimation for the root mean square error of approximation: Sample size planning for narrow confidence intervals. *Multivariate Behav. Res.* **46**, 1–32 (2011).